

Article

# Synthesis, Characterization of Nanosized $\text{ZnCr}_2\text{O}_4$ and Its Photocatalytic Performance in the Degradation of Humic Acid from Drinking Water

Raluca Dumitru <sup>1,\*</sup>, Florica Manea <sup>1</sup>, Cornelia Păcurariu <sup>1</sup>, Lavinia Lupa <sup>1</sup> , Aniela Pop <sup>1</sup>, Adrian Cioabla <sup>2,\*</sup>, Adrian Surdu <sup>3</sup> and Adelina Ianculescu <sup>3</sup>

<sup>1</sup> Faculty for Industrial Chemistry and Environmental Engineering, Politehnica University Timisoara, Piata Victoriei No. 2, Timisoara 300006, Romania; florica.manea@upt.ro (F.M.); cornelia.pacurariu@upt.ro (C.P.); lavinia.lupa@upt.ro (L.L.); aniela.pop@upt.ro (A.P.)

<sup>2</sup> Faculty of Mechanical Engineering, Politehnica University Timisoara, 1 Mihai Viteazu Blv., Timisoara 300222, Romania

<sup>3</sup> Department of Oxide Materials Science and Engineering, Faculty of Applied Chemistry and Materials Science, Polytechnic University of Bucharest, Gh. Polizu Street No.1-7, Bucharest 011061, Romania; adrian.surdu@live.com (A.S.); a\_ianculescu@yahoo.com (A.I.)

\* Correspondence: ralucadumitru2002@yahoo.com (R.D.); adrian.cioabla@upt.ro (A.C.); Tel.: +40-256-404-188 (R.D.)

Received: 31 March 2018; Accepted: 12 May 2018; Published: 15 May 2018



**Abstract:** Zinc chromite ( $\text{ZnCr}_2\text{O}_4$ ) has been synthesized by the thermolysis of a new Zn(II)-Cr(III) oxalate coordination compound, namely  $[\text{Cr}_2\text{Zn}(\text{C}_2\text{O}_4)_4(\text{OH}_2)_6] \cdot 4\text{H}_2\text{O}$ . The coordination compound has been characterized by chemical analysis, infrared spectroscopy (IR), and thermal analysis. The zinc chromite obtained after a heating treatment of the coordination compound at 450 °C for 1 h has been investigated by XRD, FE-SEM, TEM/HR-TEM coupled with selected area electron diffraction (SAED) measurements. The photocatalytic performance of nanosized zinc chromite was assessed for the degradation and mineralization of humic acid (HA) from a drinking water source, envisaging the development of the advanced oxidation process for drinking water treatment technology. A mineralization efficiency of 60% was achieved after 180 min of 50 mg L<sup>-1</sup> HA photocatalysis using zinc chromite under UV irradiation, in comparison with 7% efficiency reached by photolysis.

**Keywords:** zinc chromite; photocatalysis activity; oxalate; humic acid

## 1. Introduction

Zinc chromite ( $\text{ZnCr}_2\text{O}_4$ ), a mixed oxide that exhibits a normal spinel structure and crystallizes in the cubic system, has attracted considerable interest in material science, due to its physical-chemical properties suitable for various applications. Many applications of the nanocrystalline  $\text{ZnCr}_2\text{O}_4$  spinel have been reported, e.g., as catalytic material for a variety of reactions [1–3], a photocatalyst [4–7], a sensor for toxic gases [8], and for humidity [9,10].

The solid state reactions that consist of the mixing of oxides or carbonates, followed by calcination and grinding, are considered the most general method for preparing spinel [11–13]. A higher temperature of calcination (>1000 °C) is needed for the reactions' completion, which leads to the obtaining of spinel powder with a small surface area [14,15]. Various synthesis methods, such as co-precipitation [16,17], sol-gel [6,18], thermolysis of polymer-metal complex [19], microwave [14,20], and hydrothermal methods [15,21,22] have been investigated in order to obtain spinel powders with higher specific surface areas. Among all these methods, the most efficient one, which considers the lack of stoichiometry control and allows the formation of homogeneous nanoparticles with very good

properties for catalytic and photocatalytic usage, is considered to be synthesis at a low temperature, starting from different precursors [23–25].

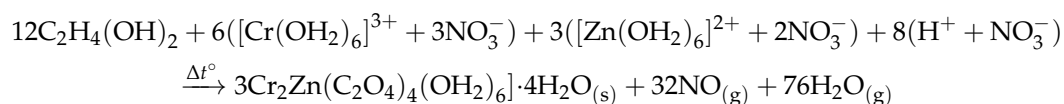
In recent years, photocatalytic oxidation as an advanced oxidation process with semiconducting materials has been studied for both water and wastewater treatment. The most studied research has considered TiO<sub>2</sub>-based materials [26–28], and recently, chromite-type materials have raised a high interest due to their certain peculiarities for photocatalysis applications, e.g., small band-gap energy and chemical stability [29,30]. ZnCr<sub>2</sub>O<sub>4</sub> is considered a very important spinel compound, due to its potential application as an efficient catalyst, and its photocatalytic activity has been reported for the removal of organic dyes from wastewaters [6,31].

The goal of this research is to obtain nanosized ZnCr<sub>2</sub>O<sub>4</sub> through this new and efficient method, based on the thermal conversion at 450 °C of the [Cr<sub>2</sub>Zn(C<sub>2</sub>O<sub>4</sub>)<sub>4</sub>(OH<sub>2</sub>)<sub>6</sub>]·4H<sub>2</sub>O precursor, and to study the compound's photocatalytic activity during the removal process of humic acid from drinking waters. This proposed method of zinc chromite spinel synthesis exhibits the advantages of a short reaction time, low reaction temperatures, no by-product generation, environmentally friendliness, and the ability to be easily scaled up due to its simplicity and low costs, compared to the conventional methods. The catalytic activity of synthesized ZnCr<sub>2</sub>O<sub>4</sub> was studied under UV irradiation for colour removal, degradation, and the mineralization of humic acids from water. Humic acids are considered to be the main component of natural organic matters (NOMs) from drinking water sources, which should be eliminated due to their potential toxicity and carcinogenic character in particular, during the disinfection step. The photocatalytic study was conducted in comparison with the photolysis process, and considered a prior sorption step before photocatalysis to assess the contribution of each process.

## 2. Results and Discussion

### 2.1. Synthesis and Characterization of the Cr<sup>3+</sup>-Zn<sup>2+</sup> Coordination Compound

The synthetic route developed for the synthesis of the coordination compound precursor is based on the redox reaction between 1,2-ethanediol and a nitrate ion in the presence of nitric acid (2M):



The IR spectrum of the oxalate precursor (Figure 1a and Table S1 Electronic Supplementary Material) displays a strong band at 1622 cm<sup>-1</sup>, attributed to ν<sub>asym(OCO)</sub> vibration, and the bands at 1391 cm<sup>-1</sup> and 910 cm<sup>-1</sup> attributed to ν<sub>sym(OCO)</sub> confirm that the ligand acts as a bidentate [32,33].

The strong band at 1719 cm<sup>-1</sup>, assigned to the ν<sub>asym(O=C-O)</sub> vibration, as well as the band at 1268 cm<sup>-1</sup> attributed to ν<sub>sym(O=C-O)</sub>, confirms that the ligand acts as a tetradentate [34,35].

The broad and intense band with the maximum at 3565 cm<sup>-1</sup> assigned to vibration ν<sub>(OH)</sub> confirms the presence of water in the Cr(III)-Zn(II) oxalate [34–36].

The IR spectrum of the ligand (Figure 1b and Table S2 Electronic Supplementary Material) is similar to the one reported by the literature for oxalic acid [33].

The thermal decomposition of the coordination compound (Figure 2) occurs in the 25–450 °C temperature range, and is characterized by a four-stage mass loss. During the first endothermic step (25–150 °C, mass loss (found/calc.) = 9.75/10.26%) is eliminated the lattice water. The second decomposition stage (150–321 °C, mass loss (found/calc.) = 14.83/15.39%) corresponds to the removal of the six coordinated molecules of water. The oxidative degradation of oxalate occurs in the third step (321–406 °C), and the mass loss ((found/calc.) = 40.69/41.06%) indicates the obtaining of a mixture of oxides: zinc oxide and nonstoichiometric oxide Cr<sub>2</sub>O<sub>3+x</sub>, x = 0.25. This assumption is supported by the existence of the fourth decomposition stage (406–450 °C). In this decomposition process, the continuous mass loss assigned to oxygen evolving is in agreement with the data from literature [35,37], and represents the formation of Cr<sub>2</sub>O<sub>3</sub> followed by obtaining the zinc chromite.

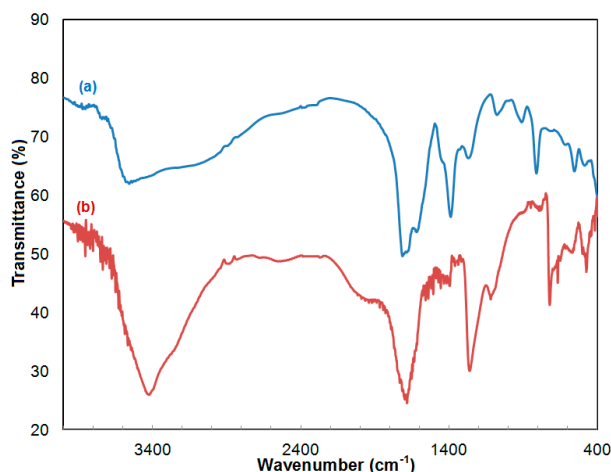


**Figure 1.** IR vibrational spectra of (a) the  $[\text{Cr}_2\text{Zn}(\text{C}_2\text{O}_4)_4(\text{OH}_2)_6]\cdot 4\text{H}_2\text{O}$  compound and (b) isolated oxalic acid.

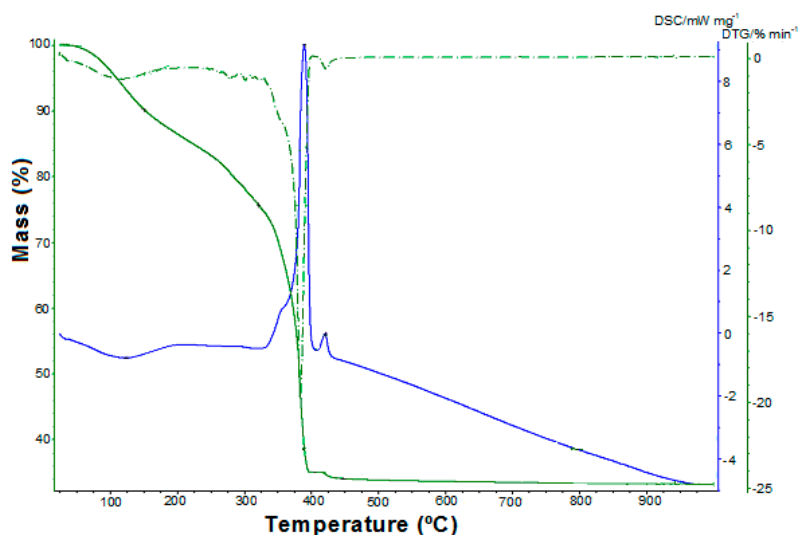
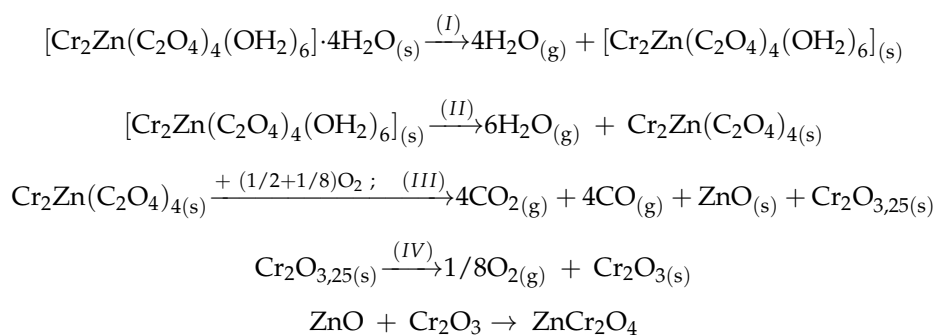


**Figure 2.** Thermal curves (TG, DTG and DSC) of  $[\text{Cr}_2\text{Zn}(\text{C}_2\text{O}_4)_4(\text{OH}_2)_6]\cdot 4\text{H}_2\text{O}$  in air atmosphere.

Based on TG, DTG and DSC curves analysis, the thermal decomposition of  $[\text{Cr}_2\text{Zn}(\text{C}_2\text{O}_4)_4(\text{OH}_2)_6]\cdot 4\text{H}_2\text{O}$  in air atmosphere can be represented by the following sequence:



The obtained zinc chromite at 480 °C was confirmed through elemental analysis ( $\text{ZnCr}_2\text{O}_4$ , calc./found: Zn% = 28.01/28.24; Cr% = 44.55/44.48).

## 2.2. Characterization of ZnCr<sub>2</sub>O<sub>4</sub> Powders

XRD investigations at room temperature performed on the powders resulting after calcination at various temperatures indicate that the crystallization process is already in progress starting with temperatures above 450 °C (Figure 3). Thus, the powder obtained after calcination at 450 °C is already crystallized, consisting of ZnCr<sub>2</sub>O<sub>4</sub> with the typical cubic spinel structure (space group Fd-3m), identified as a unique phase with the ICDD card no. 01-079-5291. The diffraction peaks of ZnCr<sub>2</sub>O<sub>4</sub> become sharper as the calcination temperature increases (Figure 3). This evolution is very similar to that reported by Gingasu et al. for their zinc chromite powders, synthesized by using the precursor method via thermal decomposition of tartarate/gluconate compounds [24].

From the structural point of view, an obvious increase of lattice parameter *a* and unit cell volume *V* takes place with the increase of the thermal treatment temperature from 450 to 600 °C, when the crystallization process is still in progress. A further rise in calcination temperature seems to no longer significantly affect the network, so that only a slight variation of the unit cell parameters and volume was observed (Table 1, Figure 3).

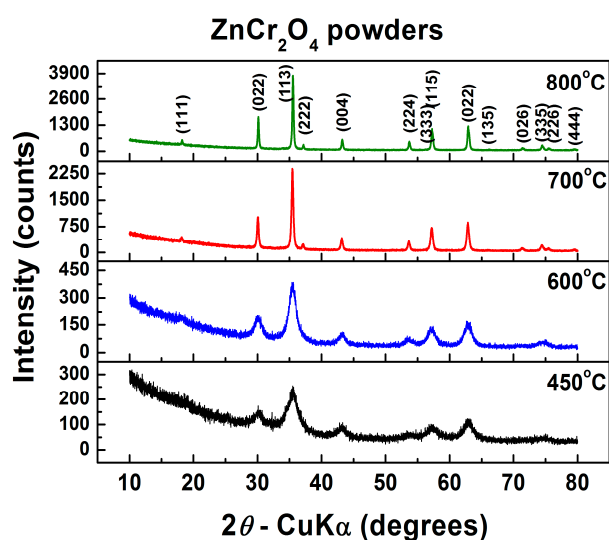


Figure 3. XRD patterns at room temperature for ZnCr<sub>2</sub>O<sub>4</sub> powders annealed at various temperatures.

Table 1. Structural parameters obtained from XRD data by Rietveld refinement (ICCD no. 01-079-5291).

Calcination Temperature	450 °C	600 °C	700 °C	800 °C
Structure/Space group	Cubic/Fd-3m			
<i>a</i> (Å)	8.3181 ± 0.0028	8.3296 ± 0.0065	8.3258 ± 0.0009	8.3295 ± 0.0005
<i>V</i> (Å <sup>3</sup> )	575.54	577.92	577.14	577.90
< <i>D</i> > (nm)	3.54 ± 0.34	5.20 ± 0.39	23.4 ± 2.26	45.79 ± 11.6
< <i>S</i> > (%)	2.85 ± 1.65	1.91 ± 0.64	0.41 ± 0.20	0.20 ± 0.04
<i>R<sub>e</sub></i>	17.43	17.60	12.88	12.44
<i>R<sub>p</sub></i>	8.02	8.83	6.50	6.46
<i>R<sub>wp</sub></i>	11.30	11.98	8.65	8.73
Goodness of fit (GOF)	0.42	0.46	3.15	0.49

As expected, the increase of the calcination temperature influenced the crystallite size *D* and lattice strain *S*. Thus, the average crystallite size increased from 3.5 nm to 45.8 nm for the ZnCr<sub>2</sub>O<sub>4</sub> powders that were thermally treated in the temperature range of 450–800 °C (Table 1). The coarsening process evolves faster at annealing temperatures above 600 °C. However, the value of the average crystallite

size was maintained in the nanometric range even for the powder calcined at 800 °C. Concurrently, the increase of the crystallite sizes induced by higher annealing temperatures led to a structural relaxation, pointed out by the decreasing trend of the values of the lattice strains (Table 1).

The morphology of the synthesized powders calcined at various temperatures is presented in the FE-SEM images of Figure 4a–d. Figure 4a,b show that nanosized particles were obtained for the powders thermally treated at temperatures ranging between 450–600 °C. In this case, the estimation of the shape and average size of particles is almost impossible, because they are very small and not well-defined, exhibiting a high agglomeration tendency. The  $\text{ZnCr}_2\text{O}_4$  powder annealed at 700 °C exhibits a duplex morphology, consisting of a large fraction of rounded, small particles of a few tens of nanometers (10–30 nm), as well as a lower proportion of polyhedral particles of 70–120 nm with well-defined edges and corners, most with an almost octahedral shape (Figure 4c). This kind of morphology was maintained in the powder calcined at 800 °C, when the coarsening process occurs for both smaller and larger particles. One can notice that, in spite of their size (of 40–50 nm), the smaller particles seem also to evolve toward a well-faceted, polyhedral shape (Figure 4d).

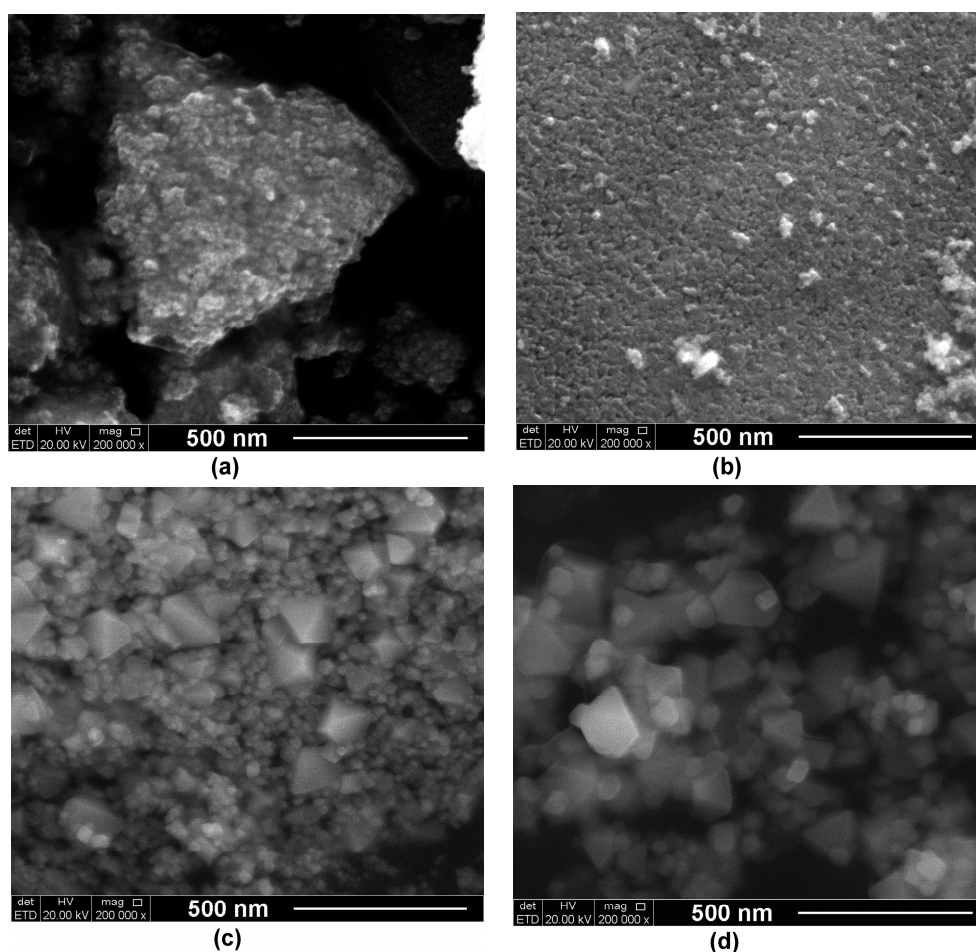


**Figure 4.** FE-SEM images showing some morphological features and the agglomeration tendency of  $\text{ZnCr}_2\text{O}_4$  powders calcined at different temperatures: (a) 450 °C; (b) 600 °C; (c) 700 °C; and (d) 800 °C.

In order to have a more realistic view of the size and morphology of the  $\text{ZnCr}_2\text{O}_4$  particles, TEM investigations are required. Thus, the TEM images of the powders annealed at lower temperatures indicate that, in both cases, the individual particles exhibit sizes of only a few nanometers. Average particle size values  $\langle d_{\text{TEM}} \rangle$  of 4.7 nm and 6.9 nm were estimated for the powders obtained after annealing at 400 and 600 °C, respectively (Figures 5a,b and 6a). These  $\langle d_{\text{TEM}} \rangle$  values fit quite well the average crystallite size values  $\langle D \rangle$  calculated from the XRD data (3.54 nm and 5.20 nm, respectively),

proving the single-crystalline nature of the  $\text{ZnCr}_2\text{O}_4$  particles, which each consist of 6–8 spinel unit cells. For the powder annealed at 700 °C, the TEM image of Figure 7a reveals the two types of particles also emphasized by the FE-SEM investigations. One can observe that some of the smaller particles already exhibit well-faceted morphology, while the larger particles seem also to be single crystals. An overall  $\langle d_{\text{TEM}} \rangle$  value of 32.5 nm was estimated for the average particle size, taking into account the two types of particles. The same tendency toward a bimodal particle size distribution was also observed in the case of the powder thermally treated at 800 °C, where a few larger octahedral particles of 120–200 nm coexist with the major fraction of smaller particles of 30–50 nm (Figure 8a,b). The overall value of the average particle size is 66.3 nm.

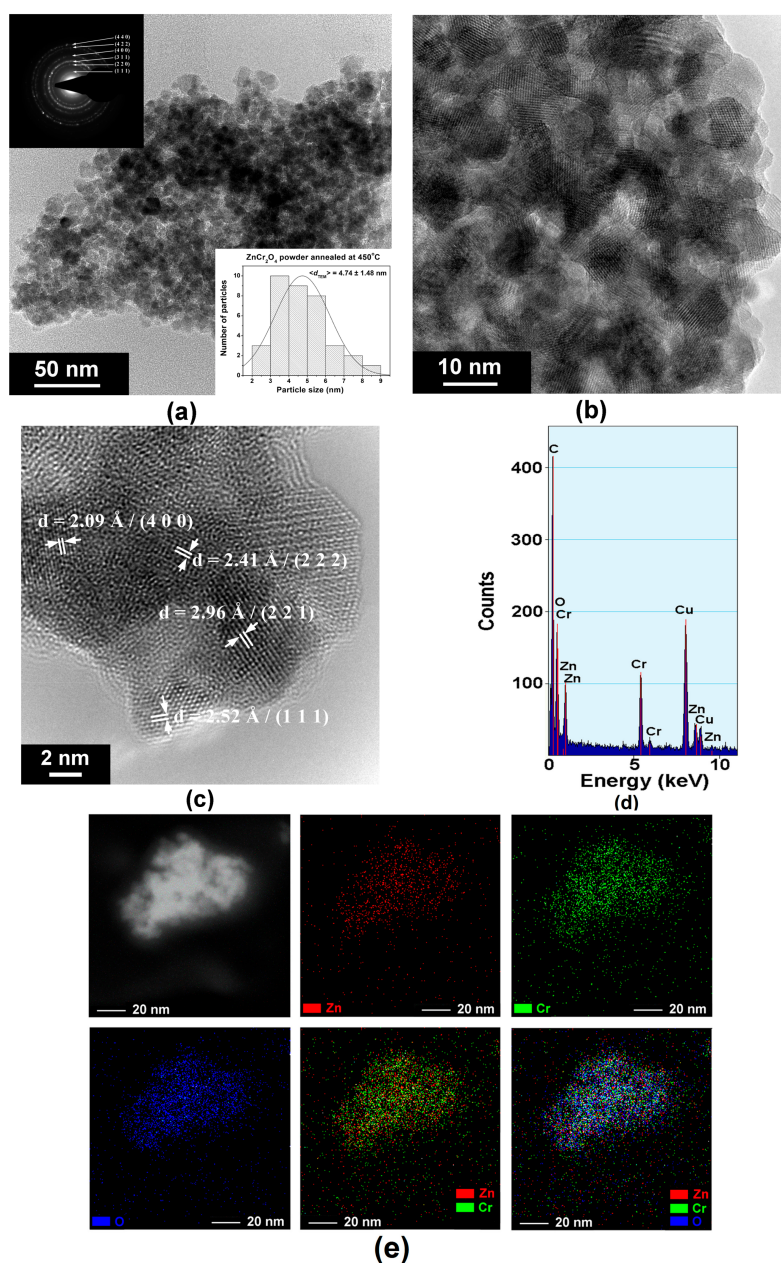


**Figure 5.** Morphology, crystallinity, and compositional uniformity of  $\text{ZnCr}_2\text{O}_4$  powder calcined at 450 °C: (a) TEM image showing a general view of a large aggregate of nanosized particles—inserts show the SAED pattern and histogram indicating the particle size distribution; (b) TEM image showing a detail inside an agglomerate; (c) HR-TEM image; (d) EDX spectrum; (e) STEM image and elemental (at. %) mapping performed on a small agglomerate of a few  $\text{ZnCr}_2\text{O}_4$  particles.

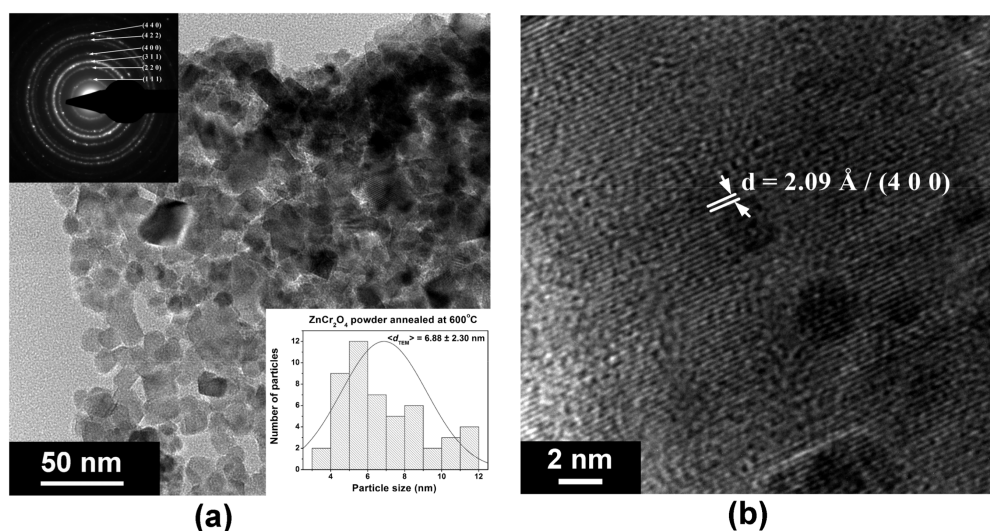


**Figure 6.** Morphology and crystallinity of  $\text{ZnCr}_2\text{O}_4$  powder calcined at  $600\text{ }^\circ\text{C}$ : (a) TEM image showing a general view of a large aggregate of nanosized particles—insets show the SAED pattern and histogram indicating the particle size distribution; (b) HR-TEM image.

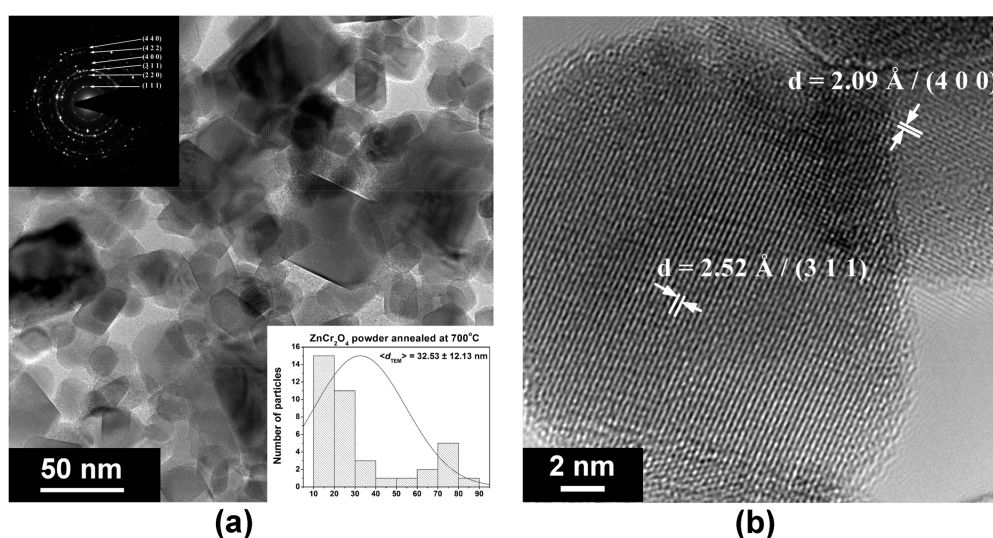


**Figure 7.** Morphology and crystallinity of  $\text{ZnCr}_2\text{O}_4$  powder calcined at  $700\text{ }^\circ\text{C}$ : (a) TEM image showing a duplex morphology consisting of a large fraction of nanosized, equiaxial particles and a small fraction of submicron, polyhedral, well-faceted particles—insets show the SAED pattern and histogram indicating the particle size distribution; (b) HR-TEM image.

Despite the small size, especially in the case of the powders thermally treated at lower temperatures ( $450$  and  $600\text{ }^\circ\text{C}$ ), the particles exhibit a high crystallinity degree, proved by the HR-TEM images of Figures 5c, 6b, 7b and 8c, which clearly show highly-ordered fringes spaced at specific distances corresponding to various crystalline planes of the spinel structure, as well as the bright spots that form well-defined diffraction rings in the SAED patterns (insets of Figures 5a, 6a, 7a and 8a).

EDX spectra of Figures 5d and 8d reveal only the presence of the Zn, Cr, and O species. No other foreign cations were identified, which proves the lack of any contamination during the synthesis process and the high purity degree of the as-prepared powdered samples.

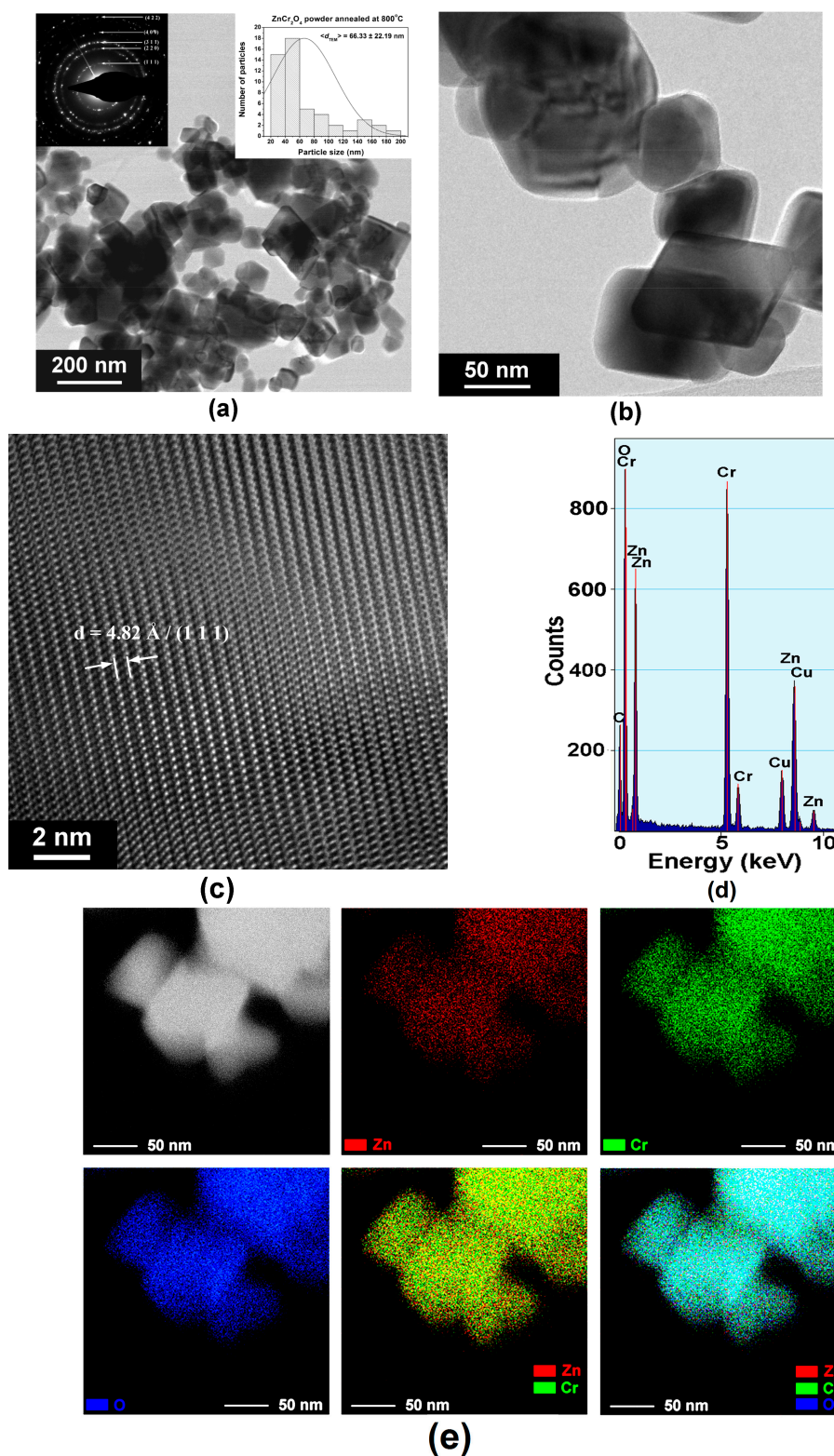


**Figure 8.** Morphology, crystallinity, and compositional uniformity of  $\text{ZnCr}_2\text{O}_4$  powder calcined at  $800\text{ }^\circ\text{C}$ : (a) TEM image showing a general view of several particles of different size and shape—insets show the SAED pattern and histogram indicating the particle size distribution; (b) TEM image showing details of a few polyhedral particles; (c) HR-TEM image; (d) EDX spectrum; (e) STEM image and elemental (at. %) mapping performed on five  $\text{ZnCr}_2\text{O}_4$  particles.

EDX mapping was carried out in order to investigate the compositional homogeneity of a small agglomerate of particles of the powder annealed at 450 °C, as well as of five larger ZnCr<sub>2</sub>O<sub>4</sub> particles of the powder annealed at 800 °C. The superposition of the maps corresponding to all three elemental species of the ZnCr<sub>2</sub>O<sub>4</sub> compound indicates a uniform distribution of Zn and Cr cations and oxygen anions, with respect to their atomic ratio in the spinel structure. This suggests that some compositional gradients or segregation of some potential secondary phases, undetected by XRD investigations, appear in the powders under investigation (Figures 5e and 8e).

Figure 9 represents, as an example, the UV-VIS diffuse reflectance spectrum of ZnCr<sub>2</sub>O<sub>4</sub> (450 °C), and a broad absorption band within a 200–650 nm wavelength can be seen. The band gap energy was determined using the Kubelka–Munk equation [38]:

$$F(R) = (1 - R)^2 / 2R, \quad (1)$$

where R is reflectance.

To determine the band gap energy, the  $(F(R)h\nu)^2-h\nu$  dependence is presented in the inset of Figure 6, where  $h\nu = 1240/\lambda$ , which determines the band gap energy value of 2.45 eV, lower than the 2.9 eV reported by Abbasi et al., [17] for ZnCr<sub>2</sub>O<sub>4</sub> and ZnCr<sub>2</sub>O<sub>4</sub>/Ag. Therefore, the results of the band gap energy values for the ZnCr<sub>2</sub>O<sub>4</sub> powder calcinated at 600, 700, and 800 °C are gathered in Table 2, and the values are larger in comparison to ZnCr<sub>2</sub>O<sub>4</sub> (450 °C). The particle size affects the band gap energy value in relation to composition, crystallinity, and crystallite size. The band gap energy decreasing as crystallite size decreases has been also reported by Irfan et al. [39]. This result showed the high photocatalytic potential of the material under both UV and VIS irradiation up to the 650 nm wavelength.

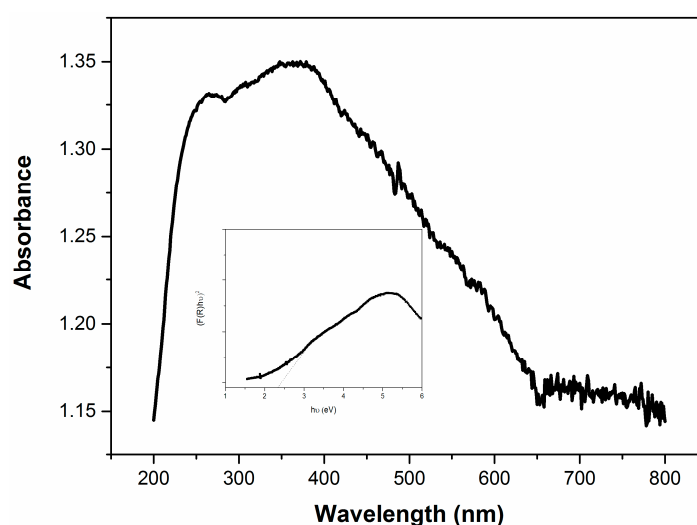


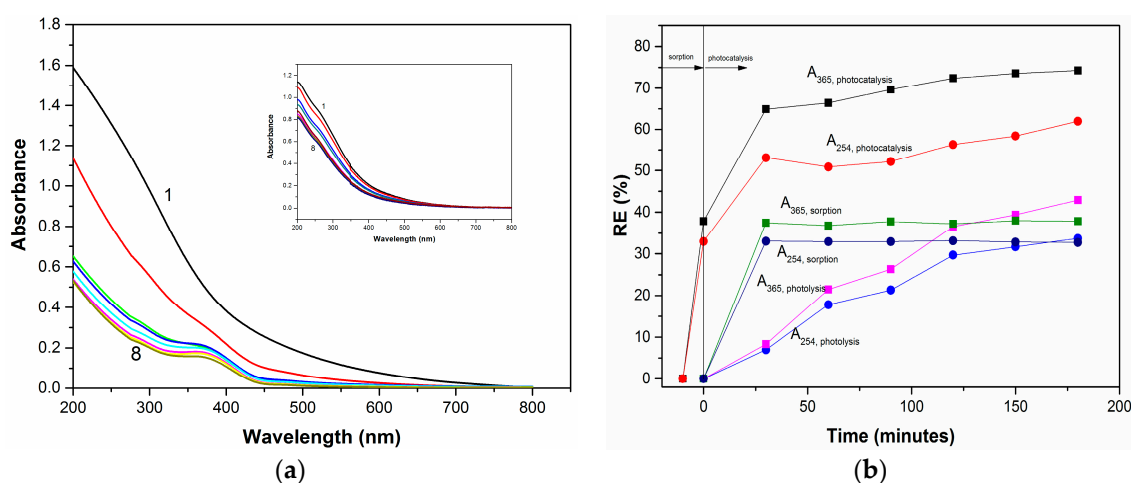
Figure 9. DRUV-VIS diffuse reflectance spectrum of ZnCr<sub>2</sub>O<sub>4</sub>. The inset shows the  $(F(R)h\nu)^2-h\nu$  plot.

Table 2. The band gap energy values of ZnCr<sub>2</sub>O<sub>4</sub>.

Calcination Temperature/°C	The Band Gap Energy Values/eV
450	2.90
600	3.19
700	3.22
800	3.25

### 2.3. Photocatalysis Activity

The initial UV-VIS spectrum profile for 50 mg/L HA and its evolution during the photocatalysis using  $\text{ZnCr}_2\text{O}_4$  (450 °C) is shown in Figure 10a, in comparison to the photolysis process (inset of Figure 10a). Absorbance recorded at wavelengths 254 nm and 365 nm is considered to be a suitable parameter for the characterization of aquatic humic substances, selected due to the fact that they indicate the presence of aromatic compounds. The aromatic compounds derived from an aquatic heterotrophic metabolism consist of nitrogen-based functions characterized by the chromophore characteristics. The comparative results of photocatalysis involving the prior sorption step for 30 min, photolysis under UV irradiation, and sorption under dark conditions, as well as the application results applied for HA removal from water expressed as RE (%), are shown in Figure 10b.



**Figure 10.** Evolution of UV-VIS spectrum profile of 50 mg/L humic acid (HA) during photocatalysis using  $\text{ZnCr}_2\text{O}_4$ . Inset shows the evolution of UV-VIS spectrum profile of 50 mg/L HA during the photocatalysis (a) and the removal efficiency (RE) evolution for 50 mg/L HA removal from water by application of sorption-based photocatalysis (solid line) and photolysis (dash line), assessed in terms of  $A_{254}$  and  $A_{365}$  (b).

It is obvious that  $\text{ZnCr}_2\text{O}_4$ -based photocatalysis enhanced the humic acid (HA) degradation in comparison with photolysis. Also, it can be seen that after adsorption for 30 min, the HA removal efficiency of about 30% was reached. Once the UV irradiation process started, a very significant decrease in the HA spectrum intensity was observed. It is noteworthy that during photocatalysis application, two distinct rate steps were delimited, except the sorption stage. The first one was characterised by a fast kinetics rate until 30 min of photocatalysis, followed by slower kinetics rate. Thus, for 30 min of the photocatalysis, a synergic effect regarding removal efficiency was found that was related to the sorption and the photolysis effect. This aspect denoted a good photocatalytic capacity of  $\text{ZnCr}_2\text{O}_4$  for HA degradation that also considers the sorption effect as a compulsory stage in the photocatalytic mechanism. A different behaviour is observed for the photolysis application, which is characterised by a constant slow kinetics rate. The sorption characteristics of the  $\text{ZnCr}_2\text{O}_4$  photocatalyst have been proved by kinetics modelling. The pseudo-first kinetics model was used to fit the experimental results for both photolysis and the photocatalysis, but the low correlation coefficient obtained for the photocatalysis showed that this model did not describe precisely. The second-order kinetics model better fit the experimental results for the photocatalysis application, which corresponded mainly to the sorption process, thus indicating a major contribution of sorption within the photocatalysis. A longer irradiation time in the presence of  $\text{ZnCr}_2\text{O}_4$  indicated the slow kinetics of the photocatalysis process, and at its peak the cumulating effect of sorption and

photolysis processes was noticed. The first-order kinetics model described the photocatalysis very well, and the results related to the rate constants are given in Table 3.

**Table 3.** Apparent rate constants calculated by fitting experimental data through the pseudo-second-order kinetics model for photocatalysis and the pseudo-first-order kinetics model for photolysis.

Process/Catalyst	Parameters	Value/Absorbance	
		A <sub>254</sub>	A <sub>365</sub>
Photocatalysis/ZnCr <sub>2</sub> O <sub>4</sub>	K <sub>app</sub> (g mg <sup>-1</sup> min <sup>-1</sup> )	4·10 <sup>-3</sup>	16.2·10 <sup>-3</sup>
	R <sup>2</sup>	0.997	0.988
Photolysis	K <sub>app</sub> (min <sup>-1</sup> )	2.1·10 <sup>-3</sup>	2.9·10 <sup>-3</sup>
	R <sup>2</sup>	0.923	0.937

As we mentioned already, based on the RE the kinetics results sustained ZnCr<sub>2</sub>O<sub>4</sub> as a photocatalyst for UV irradiation for humic acid removal. Moreover, to support this statement, the mineralization degree was assessed by the total organic carbon (TOC) parameter for both photocatalysis and photolysis. The mineralization degree was about 60% for photocatalysis, compared to 7% for photolysis and 30% for sorption, which showed a net superiority of ZnCr<sub>2</sub>O<sub>4</sub> for HA mineralization. Also, the mineralization degree is very close to the degradation efficiency that confirmed the effectiveness of the HA mineralization through photocatalysis, using the ZnCr<sub>2</sub>O<sub>4</sub> photocatalyst. Based on these results, it can be concluded that a complex mechanism of HA degradation is based on sorption in the first stage and on mineralization through hydroxyl radicals generated under UV irradiation [26].

### 3. Materials and Methods

For the synthesis of the Zn(II)-Cr(III) oxalate coordination compound, Cr(NO<sub>3</sub>)<sub>3</sub>·9H<sub>2</sub>O, Zn(NO<sub>3</sub>)<sub>2</sub>·6H<sub>2</sub>O, 1,2-ethanediol, and 2M nitric acid (Merck) were employed.

A water solution containing 1,2-ethanediol, chromium nitrate, zinc nitrate, and nitric acid (2M) in a molar ratio 2:1:0.5:1.3 was used. This mixture was heated in a water bath for about 40 min. The reaction was finished when no more gas evolved. The resulting solid product was purified by washing with acetone and dried under a room temperature environment. The metal content was determined by the atomic absorption spectrophotometry (VARIAN Spectra 110 spectrophotometer). Carbon and hydrogen were analyzed using a Carlo Erba 1108 elemental analyzer. The data of the elemental analysis for the oxalate precursor is indicated in the Table 4.

**Table 4.** Composition and elemental analysis data.

Compound	Cr(III) %		Zn(II) %		C %		H %	
	calc.	found	calc.	found	calc.	found	calc.	found
(composition formula) Cr <sub>2</sub> Zn(C <sub>2</sub> O <sub>4</sub> ) <sub>4</sub> ·10H <sub>2</sub> O	14.82	14.90	9.32	9.25	13.68	13.70	2.85	2.91

In order to identify the ligand, the Cr<sup>3+</sup>-Zn<sup>2+</sup> oxalate was treated with R-H cationite (Purolite C-100). After the metallic cations were retained and the remained solution evaporated, the solid oxalic acid (H<sub>2</sub>C<sub>2</sub>O<sub>4</sub>·2H<sub>2</sub>O) was obtained. The isolated ligand was identified through three procedures: elemental analysis (H<sub>2</sub>C<sub>2</sub>O<sub>4</sub>·2H<sub>2</sub>O, calc./found: C% = 19.04/19.22; H% = 4.76/4.98), FTIR spectroscopy (Figure 1b and Table S2 Electronic Supplementary Material), and specific reactions [32].

FTIR spectra (KBr pellets) of the compound and of the decomposition product were recorded on a Jasco FT-IR spectrophotometer, in the range of 4000–400 cm<sup>-1</sup>. Thermal measurements (TG, DTG, and DSC) were performed using a NETZSCH-STA 449C instrument, in the range of 25–1000 °C, using alumina crucibles. The experiments were carried out in artificial air flow of 20 mL min<sup>-1</sup> and a heating

rate of  $10 \text{ K min}^{-1}$ . The phase purity and crystal structure of  $\text{ZnCr}_2\text{O}_4$  powders were determined by X-ray diffraction (XRD) investigations, performed at room temperature by means of a Rigaku Ultima IV multipurpose diffraction system (Rigaku Co., Tokyo, Japan). The diffractometer was set in a parallel beam geometry, using Ni-filtered  $\text{CuK}\alpha$  radiation ( $\lambda = 1.5418 \text{ \AA}$ ), CBO optics, and a graphite monochromator, operated at 40 kV and 40 mA. The measurements were performed in  $\theta$ - $2\theta$  mode, with a scan step increment of  $0.01^\circ$ , in the  $2\theta$  range of ( $10^\circ$ – $80^\circ$ ). Phase identification was performed using HighScore Plus 3.0e software, connected to the ICDD PDF-4+ 2017 database. Lattice parameters were refined by the Rietveld method. After removing the instrumental contribution, the full-width at half-maximum (FWHM) of the diffraction peaks can be interpreted in terms of crystallite size and lattice strain. A pseudo-Voigt function was used to refine the shapes of the  $\text{ZnCr}_2\text{O}_4$  peaks, and a Caglioti function was used for FWHM approximation. The size and the agglomeration tendency of the  $\text{ZnCr}_2\text{O}_4$  particles was assessed by scanning electron microscopy (FE-SEM), using a high-resolution FEI QUANTA INSPECT F microscope with field emission gun (FEI Co., Eindhoven, The Netherlands). For a high-accuracy estimation of the morphology and crystallinity degree of the  $\text{ZnCr}_2\text{O}_4$  particles, additional transmission electron microscopy (TEM/HR-TEM) and selected area electron diffraction (SAED) investigations were performed. The bright-field and high resolution images, as well as the SAED patterns, were collected by means of a TecnaiTM G<sup>2</sup> F30 S-TWIN transmission electron microscope (FEI Co., Eindhoven, The Netherlands). An image-corrected 80–200 kV Titan Themis transmission and scanning transmission electron microscope (S/TEM), equipped with a high brightness Schottky field emission gun (X-FEG) tip and a four diode Super X-ray energy dispersive spectroscopy (X EDS) detector (Thermo Fisher Scientific, former FEI Co., Eindhoven, Netherlands) was used for rapid compositional analyses (acquisition of STEM images and EDX mappings). For these purposes, small amounts of powdered samples were suspended in ethanol by 15 min ultrasonication. For FE-SEM analyses, a drop of the suspension was put on a carbon tape stuck on a stub and dried under an IR lamp for 5 min. Finally, the sample was sputtered with a gold film. For TEM observations, a drop of suspension was put onto a 400 mesh holey carbon-coated film Cu grid and dried. The average particle size for the  $\text{ZnCr}_2\text{O}_4$  powders was determined using the OriginPro 9.0 software, by taking into account size measurements on 50–60 particles (from TEM images of appropriate magnifications obtained from various microscopic fields), performed by means of the microscope software DigitalMicrograph 1.8.0. The UV-Vis diffuse reflectance spectrum of the zinc chromite was obtained on a UV-VIS Carry 100 Varian spectrophotometer.

The photocatalytic experiments were carried out under magnetic stirring at  $20^\circ\text{C}$  into a RS-1 photocatalytic reactor (Heraeus, Hanau, Germany), which consisted of a submerged UV lamp surrounded by a quartz shield. For each experiment, an adsorption step of 30 min was assured under the same hydrodynamic conditions without UV irradiation. At a certain running time, the suspension was sampled and filtered through a  $0.4 \mu\text{m}$  membrane filter. The concentration of humic acid was measured in terms of absorbance at 254 nm ( $A_{254}$ ) and at 345 nm ( $A_{345}$ ), in order to evaluate the decolorizing and respective degradation degrees, using a Carry 100 Varian spectrophotometer. Humic acid has a very complex structure, containing heterogeneous mixtures of small molecules, which usually result from the biological transformations of dead cells associated with a supramolecular structure that can be separated into smaller molecules by chemical fractionation.

To assess the mineralization degree, the total organic carbon (TOC) parameter was measured for initial and final HA concentration, using the TOC analyzer from Shimadzu (Tokyo, Japan). The HA removal efficiency was calculated using the following equation:

$$\text{Removal efficiency (RE)} = \frac{C_0 - C_t}{C_0} \times 100 (\%) \quad (2)$$

where  $C_0$  and  $C_t$  are the concentrations of HA in aqueous solution, in terms of the  $A_{254}$ ,  $A_{345}$ , and TOC parameters at initial time and certain time  $t$ , respectively ( $\text{mg L}^{-1}$ ). Kinetics data were fitted with the pseudo-second-order kinetic model [28], and expressed as:

$$\frac{t}{q_t} = \frac{1}{k_2 \cdot q_e^2} + \frac{t}{q_e}, \quad (3)$$

where  $k_2$  is the rate constant of the pseudo-second-order adsorption kinetics ( $\text{g mg}^{-1} \text{min}^{-1}$ ) and  $q_e$  is the equilibrium adsorption capacity ( $\text{mg g}^{-1}$ ). The simplified pseudo-first-order equation was used also, to fit the kinetics data:

$$\ln(C_0/C_t) = kKt = k_{app}t, \quad (4)$$

where  $r$  is the rate of humic acid degradation and colour removal ( $\text{mg L}^{-1} \text{min}^{-1}$ ),  $C_0$  is the initial humic acid concentration ( $\text{mg L}^{-1}$ ),  $C_t$  is the concentration of the humic acid at time  $t$  ( $\text{mg L}^{-1}$ ),  $t$  is the irradiation time (min), and  $k$  is the reaction rate constant ( $\text{min}^{-1}$ ).

#### 4. Conclusions

Nanospinel zinc chromite was successfully synthesized using a new method, via thermal decomposition of the  $[\text{Cr}_2\text{Zn}(\text{C}_2\text{O}_4)_4(\text{OH}_2)_6] \cdot 4\text{H}_2\text{O}$  oxalate compound at the temperature of  $450^\circ\text{C}$ . XRD investigations, FE-SEM, and TEM/HR-TEM analyses indicated that phase-pure  $\text{ZnCr}_2\text{O}_4$  nanoparticles were obtained after calcination at temperatures ranging between  $450\text{--}800^\circ\text{C}$ . The average particle size values increased with increasing temperature, from  $4.7 \text{ nm}$  ( $450^\circ\text{C}$ ) to  $66.3 \text{ nm}$  ( $800^\circ\text{C}$ ), which affected the band gap energy value. The lowest band gap energy value of  $2.45 \text{ eV}$  was determined for the  $\text{ZnCr}_2\text{O}_4$  powder after calcination at  $450^\circ\text{C}$ , which exhibited photocatalytic activity towards the degradation and the mineralization of humic acids (HAs) from water. The sorption efficiency of this spinel for HAs was about 30% after 30 min, and the photocatalytic efficiency for HA degradation was about 60%, which was similar to the mineralization degree, thus confirming the effectiveness of photocatalysis for mineralization while avoiding the generation of by-products. The sorption step was confirmed by the pseudo-second-order kinetics model to fit the experimental results best, which is characteristic to sorption in comparison with the photocatalysis process, which was described as the best by the pseudo-first kinetics model. Two steps of the photocatalysis process using nanosized  $\text{ZnCr}_2\text{O}_4$  spinel were found: the first step was characterized by the fast rate, while the second step occurred at the slow rate. In comparison with the photolysis and sorption process, a synergic effect was found for the photocatalysis process during the first 30 min. Then, a maximum cumulative effect was found until 180 min. Taking into account the energy consumption that corroborates these study results, the optimum irradiation time of the photocatalysis with  $\text{ZnCr}_2\text{O}_4$  is 30 min. This study informed about the great potential of this spinel to be used for drinking water treatment via its photocatalytic application.

**Supplementary Materials:** The following are available online at <http://www.mdpi.com/2073-4344/8/5/210/s1>, Table S1: Characteristic IR absorption bands of the compound  $[\text{Cr}_2\text{Zn}(\text{C}_2\text{O}_4)_4(\text{OH}_2)_6] \cdot 4\text{H}_2\text{O}$ , Table S2: Characteristic IR absorption bands of the oxalic acid.

**Author Contributions:** In this paper, R.D. and F.M. conceived and designed the experiments; C.P., L.L., A.P. and A.S. performed the experiments; R.D., F.M., A.P., A.C. and A.I. analyzed the data; A.C. contributed reagents/materials/analysis tools; R.D., F.M. and A.I. wrote the paper.

**Acknowledgments:** This work was partially supported by a grant of the Romanian National Authority for Scientific Research and Innovation, CNCS-UEFISCDI, project number PN-II-RU-TE-2104-4-1043. The TEM characterization was possible due to EU-funding project POSCCE-A2-O2.2.1-2013-1/Priority Axe 2, Project No. 638/12.03.2014, ID 1970, SMIS-CSNR code 48652. The contribution of Bogdan Vasile in performing some TEM/EDX investigations is highly acknowledged.

**Conflicts of Interest:** The authors declare no conflict of interest.

## References

1. Gabr, R.M.; Girgis, M.M.; El-Awad, A.M. Formation, conductivity and activity of zinc chromite catalyst. *Mater. Chem. Phys.* **1992**, *30*, 6619–6623. [[CrossRef](#)]
2. Epling, W.S.; Hoflund, G.B.; Minahan, D.M. Reaction and surface characterization study of higher alcohol synthesis catalysts: VII Cs- and Pd-promoted 1:1 Zn/Cr spinel. *J. Catal.* **1998**, *175*, 175–184. [[CrossRef](#)]
3. El-Sharkawy, E.A. Textural, structural and catalytic properties of ZnCr<sub>2</sub>O<sub>4</sub>/Al<sub>2</sub>O<sub>3</sub> catalysts. *Adsorpt. Sci. Technol.* **1998**, *6*, 193–216. [[CrossRef](#)]
4. Peng, C.; Gao, L. Optical and photocatalytic properties of spinel ZnCr<sub>2</sub>O<sub>4</sub> nanoparticles synthesized by a hydrothermal route. *J. Am. Soc.* **2008**, *91*, 2388–2390. [[CrossRef](#)]
5. Thennarasu, G.; Sivasamy, A. Synthesis and characterization of nanolayered ZnO/ZnCr<sub>2</sub>O<sub>4</sub> metal oxide composites and its photocatalytic activity under visible light irradiation. *J. Chem. Technol. Biotechnol.* **2015**, *90*, 514–524. [[CrossRef](#)]
6. Yazdanbakhsh, M.; Khosravi, I.; Goharshadi, E.K.; Youssefi, A. Fabrication of nanospinel ZnCr<sub>2</sub>O<sub>4</sub> using sol-gel method and its application on removal of azo-dye from aqueous solutions. *J. Hazard. Mater.* **2010**, *184*, 684–689. [[CrossRef](#)] [[PubMed](#)]
7. He, H.Y. Catalytic and photocatalytic activity of ZnCr<sub>2</sub>O<sub>4</sub> particle synthesized using metallo-organic precursor. *Mater. Technol.* **2008**, *23*, 110–113. [[CrossRef](#)]
8. Niu, X.; Du, W.; Du, W. Preparation and gas sensing properties of ZnM<sub>2</sub>O<sub>4</sub> (M = Fe, Co, Cr). *Sens. Actuators B* **2004**, *99*, 405–409. [[CrossRef](#)]
9. Pokhrel, S.; Jeyaraj, B.; Nagaraja, K.S. Humidity-sensing properties of ZnCr<sub>2</sub>O<sub>4</sub>-ZnO composites. *Mater. Lett.* **2003**, *57*, 3534–3548. [[CrossRef](#)]
10. Bayahn, M.; Hashemi, T.; Brinkman, A.W. Sintering and humidity-sensitive behavior of the ZnCr<sub>2</sub>O<sub>4</sub>-K<sub>2</sub>CrO<sub>4</sub> ceramic system. *J. Mater. Sci.* **1997**, *32*, 6619–6623. [[CrossRef](#)]
11. Marinkovic Stanojevic, Z.V.; Mancic, L.; Marcic, L.; Milosevici, O. Microstructural characterization of mechanically activated ZnO-Cr<sub>2</sub>O<sub>3</sub> system. *J. Eur. Ceram. Soc.* **2005**, *25*, 2081–2084. [[CrossRef](#)]
12. Marinkovic Stanojevic, Z.V.; Romcevic, N.; Stoganovic, B. Spectroscopic study of spinel ZnCr<sub>2</sub>O<sub>4</sub> obtained from mechanically activated ZnO-Cr<sub>2</sub>O<sub>3</sub> mixtures. *J. Eur. Ceram. Soc.* **2007**, *27*, 903–907. [[CrossRef](#)]
13. Imelda, E.; Myriam, P.; Roberto, M.; Adriana, G.C.; Guadalupe, S.L.; Luisa, M.F.V.; Octavia, D. Solid state reaction in Cr<sub>2</sub>O<sub>3</sub>-ZnO nanoparticles synthesized by triethanolamine chemical precipitation. *Mater. Sci. Appl.* **2011**, *2*, 1584–1592. [[CrossRef](#)]
14. Mousavi, Z.; Esmaili-Zare, M.; Salavati-Niasari, M. Magnetic and optical properties of zinc chromite nanostructures prepared by microwave method. *Trans. Nonferr. Met. Soc. China* **2015**, *25*, 3980–3986. [[CrossRef](#)]
15. Naz, S.; Durrani, S.K.; Mehmood, M.; Nadeem, M. Hydrothermal synthesis, structural and impedance studies of nanocrystalline zinc chromite spinel oxide material. *J. Saudi. Chem. Soc.* **2016**, *20*, 585–593. [[CrossRef](#)]
16. Mousavi, Z.; Soofivand, F.; Esmaili-Zare, M.; Salavati-Niasari, M.; Bagheri, S. ZnCr<sub>2</sub>O<sub>4</sub> nanoparticles: Facile synthesis, characterization and photocatalytic properties. *Sci. Rep.* **2016**, *6*, 20071. [[CrossRef](#)] [[PubMed](#)]
17. Babar, A.R.; Kumbhar, S.B.; Shinde, S.S.; Moholkar, A.V.; Kim, J.H.; Rajpure, K.Y. Structural, compositional and electrical properties of co-precipitated zinc stannate. *J. Alloy. Comp.* **2011**, *509*, 7508–7514. [[CrossRef](#)]
18. Cui, H.; Zayat, M.; Levy, D. Sol-gel synthesis of nanoscaled spinel using propylene oxide as a gelation agent. *Sol-Gel Sci. Technol.* **2005**, *35*, 175–181. [[CrossRef](#)]
19. Gene, S.A.; Saion, E.; Shaari, A.H.; Kamarudin, M.A.; Al-Hada, N.M.; Kharazmi, A. Structural, optical and magnetic characterization of spinel zinc chromite nanocrystallines synthesized by thermal treatment methods. *J. Nanomater.* **2014**, *2014*, 416765. [[CrossRef](#)]
20. Hailiang, L.; Wenling, M.; Xiaohua, Y.; Jungi, L. Preparation and characterization of MgCr<sub>2</sub>O<sub>4</sub> nanocrystals by microwave method. *Adv. Mater. Res.* **2011**, *152*, 1000–1003. [[CrossRef](#)]
21. Durani, S.K.; Hussain, S.Z.; Saeed, K.; Khan, Y.; Arif, M.; Ahmed, H. Hydrothermal synthesis and characterization of nanosized transition metal chromite spinels. *Turk. J. Chem.* **2012**, *36*, 111–120. [[CrossRef](#)]
22. Durani, S.K.; Naz, S.; Hayat, K. Thermal analysis and phase evolution of nanocrystalline perovskite oxide materials synthesized via hydrothermal and self-combustion methods. *J. Therm. Anal. Calorim.* **2014**, *115*, 1371–1380. [[CrossRef](#)]

23. Stefanescu, M.; Barbu, M.; Vlase, T.; Barvinschi, P.; Barbu-Tudoran, L.; Stoia, M. Novel low temperature synthesis method for nanocrystalline zinc and magnesium chromites. *Thermochim. Acta* **2011**, *526*, 130–136. [[CrossRef](#)]
24. Gingasu, D.; Mindru, I.; Patron, L.; Culita, D.C.; Calderon-Moreno, J.M.; Diamandescu, L.; Feder, M.; Oprea, O. Precursor method—A nonconventional route for the synthesis of ZnCr<sub>2</sub>O<sub>4</sub> spinel. *J. Phys. Chem. Solid* **2013**, *74*, 1295–12302. [[CrossRef](#)]
25. Gingasu, D.; Mindru, I.; Culita, D.C.; Patron, L.; Calderon-Moreno, J.M.; Preda, S.; Oprea, O.; Osiceanu, P.; Pineda, E.M. Investigation of nanocrystalline zinc chromite obtained by two soft chemical routes. *Mater. Res. Bull.* **2014**, *49*, 151–159. [[CrossRef](#)]
26. Fujishima, A.; Rao, T.N.; Tryk, D.A. Titanium Dioxide Photocatalysis. *J. Photochem. Photobiol. C Photochem. Rev.* **2000**, *1*, 1–21. [[CrossRef](#)]
27. Orha, C.; Pode, R.; Manea, F.; Lazau, C.; Bandas, C. Titanium dioxide-modified activated carbon for advanced drinking water treatment. *Process Saf. Environ. Prot.* **2017**, *108*, 26–33. [[CrossRef](#)]
28. Orha, C.; Manea, F.; Pop, A.; Bandas, C.; Lazau, C. TiO<sub>2</sub>-nanostructured carbon composite sorbent/photocatalyst for humic acid removal from water. *Desalin. Water Treat.* **2016**, *57*, 14178–14187. [[CrossRef](#)]
29. Yuan, W.; Liu, X.; Li, L. Synthesis, characterization and photocatalytic activity of cubic-like CuCr<sub>2</sub>O<sub>4</sub> for dye degradation under visible light irradiation. *Appl. Surf. Sci.* **2014**, *319*, 350–357. [[CrossRef](#)]
30. Vader, V.T. Ni and Co substituted zinc ferri-chromite: A study of their influence in photocatalytic performance. *Mater. Res. Bull.* **2017**, *85*, 18–22. [[CrossRef](#)]
31. Abbasi, A.; Hamadani, M.; Salavati-Niasari, M.; Mortazavi-Derazkola, S. Facile size-controlled preparation of highly photocatalytically active ZnCr<sub>2</sub>O<sub>4</sub> and ZnCr<sub>2</sub>O<sub>4</sub>/Ag nanostructures for removal of organic contaminants. *J. Colloid Interface Sci.* **2017**, *500*, 276–284. [[CrossRef](#)] [[PubMed](#)]
32. Dumitru, R.; Papa, F.; Balint, I.; Culita, D.; Munteanu, C.; Stanica, N.; Ianculescu, A.; Diamandescu, L.; Carp, O. Mesoporous cobalt ferrite: A rival of platinum catalyst in methane combustion reaction. *Appl. Catal. A Gen.* **2013**, *467*, 178–186. [[CrossRef](#)]
33. Nakamoto, K. *Infrared and Raman Spectra of Inorganic and Coordination Compounds*; Wiley: New York, NY, USA, 1986; ISBN 0471010669.
34. Fujita, J.; Nakamoto, K.; Kobayshi, M. Infrared Spectra of Metallic Complexes. II. The Absorption Bands of Coordinated Water in Aquo Complexes. *J. Am. Chem. Soc.* **1956**, *78*, 3963–3965. [[CrossRef](#)]
35. Bîrzescu, M.; Niculescu, M.; Dumitru, R.; Carp, O.; Segal, E. Synthesis, structural characterization and thermal analysis of the cobalt(II) oxalate obtained through the reaction of 1,2-ethanediol with Co(NO<sub>3</sub>)<sub>2</sub>·6H<sub>2</sub>O. *J. Therm. Anal. Calorim.* **2009**, *96*, 979–986. [[CrossRef](#)]
36. Bîrzescu, M. Combinations with Ethyleneglycol and Their Oxidation Products. Ph.D. Thesis, University of Bucharest, Bucharest, Romania, 1998.
37. Ștefănescu, M.; Sasca, V.; Bîrzescu, M. Thermal behaviour of the homopolynuclear glyoxylate complex combinations with Cu(II) and Cr(III). *J. Therm. Anal. Calorim.* **2003**, *72*, 515–524. [[CrossRef](#)]
38. Kubelka, P.; Munk, F. Ein Beitrag Zur Optik Der Farbanstriche. *Z. Tech. Phys.* **1931**, *12*, 593–601.
39. Irfan, S.; Shen, Y.; Rizwan, S.; Wang, H.C.; Khan, S.B.; Nan, C.W. Band-gap engineering and enhanced photocatalytic activity of Sm and Mn doped BiFeO<sub>3</sub> nanoparticles. *J. Am. Ceram. Soc.* **2016**, *100*, 31–40. [[CrossRef](#)]

